Tectonophysics 853 (2023) 229801

Contents lists available at ScienceDirect

Tectonophysics

journal homepage: www.elsevier.com/locate/tecto

Large volume of magma involved in South China Sea rifting: Implication for mantle breakup earlier than crust

Jiangyang Zhang [a,b], Minghui Zhao [a,b,*], Zhen Sun [a,b,*], Longtao Sun [a,b], Min Xu [a,b], Hongfeng Yang [c], Qiang Wang [a,d], Xiong Pang [e], Jinyun Zheng [e], Yongjian Yao [f]

[a] Key Laboratory of Ocean and Marginal Sea Geology, South China Sea Institute of Oceanology, Innovation Academy of South China Sea Ecology and Environmental Engineering, Chinese Academy of Sciences, Guangzhou 511458, China
[b] Southern Marine Science and Engineering Guangdong Laboratory (Guangzhou), Guangzhou 511458, China
[c] Earth System Science Programme, The Chinese University of Hong Kong, Shatin, NT, Hong Kong, China
[d] Key Laboratory of Geohazard Prevention of Hilly Mountains of Ministry of Natural Resources of China, Fujian Geological Engineering Survey Institute, Fuzhou 350002, China
[e] CNOOC Ltd.-Shenzhen, Shenzhen, 518054, China
[f] Guangzhou Marine Geological Survey, Ministry of Land and Resources of PRC, Guangzhou 510760, China

ARTICLE INFO

Keywords:
South China Sea
Crust structure
High-velocity lower crust
P-wave velocity model
Lithospheric mantle breakup

ABSTRACT

Rheological differences may lead to discrepant thinning order of the crust and lithospheric mantle when the continent is passively stretched. The crust breaks up earlier than the lithospheric mantle under a low stretching rate when the lower crust is strong; otherwise, the lithospheric mantle may break up earlier than the crust. Here we report a new high-resolution wide-angle seismic velocity model from ocean bottom seismometers (OBS) across the northern continental margin of the South China Sea (SCS). Significant crustal structure and deformation style discrepancies are observed from the proximal to distal margin of the northern SCS. High-velocity lower crust (HVLC) up to 10 km in thickness was observed below the Yunli uplift and the oceanward margin, indicating magmatic underplating, while nearly no HVLC was found below the highly extended landward sags. Seismic data showed a low ratio of upper/lower crustal thickness below the underplating area, presumably caused by magmatic accretion and lower crustal flow. Largely seaward-dipping faults with small vertical offsets were observed on the seaward side of the HVLC. The OBS and multichannel seismic data favor a model with the lithospheric mantle breaking up prior to the crust at the SCS. Based on the observed stratigraphic relationship and volcanic rocks dating results, we conclude that erosion of the sedimentary strata is synchronous to the magmatic underplating, which indicates that lithospheric mantle breakup occurred at ~43–38 Ma. The northern central SCS breakup occurred in two steps, in which the lithospheric mantle broke up ~10 Myr earlier than the crust (at ~31–29 Ma).

1. Introduction

Rifting and eventual breakup of a continental lithosphere are essential tectonic processes to create new oceans and transport the magma and heat from the mantle to Earth's surface. Therefore, understanding how the rifted margins of various types are formed can yield important insights into the evolution of the Earth. According to differences in crustal structure and magmatic activity, rifted continental margins are typically divided into magma-rich and magma-poor end-members. Magma-rich margins are usually characterized by seaward-dipping reflected sequences (SDRs) and are associated with active mantle upwelling caused by hotspots or a very fast spreading rate (Roberts et al., 1984; Geoffroy et al., 2015). In contrast, magma-poor margins are mainly associated with passive mantle upwelling and limited magmatism (Boillot et al., 1980; Sawyer et al., 2007; Clerc et al., 2018). In the absence of mantle plumes, rheological differences may lead to discrepant mechanical behavior of the crust and lithospheric mantle after the continental lithosphere is hyper-stretched. Previous studies suggested that the strength of the lower crust and the coupling degree between crust and mantle play an essential role in the breakup

* Corresponding authors at: Key Laboratory of Ocean and Marginal Sea Geology, South China Sea Institute of Oceanology, Innovation Academy of South China Sea Ecology and Environmental Engineering, Chinese Academy of Sciences, Guangzhou 511458, China
E-mail addresses: mhzhao@scsio.ac.cn (M. Zhao), zhensun@scsio.ac.cn (Z. Sun).

https://doi.org/10.1016/j.tecto.2023.229801
Received 25 October 2022; Received in revised form 30 January 2023; Accepted 11 March 2023
Available online 20 March 2023

order of the crust and lithospheric mantle (Huismans and Beaumont, 2011; Ros et al., 2017). Generally, a strong lower crust leads to a crustal breakup before the mantle, resulting in the exhumed and serpentinized mantle at the continental-oceanic transition. In contrast, a weak lower crust favors the breakup in the lithospheric mantle rather than in the crust and usually generates magmatic underplating.

No SDR or serpentinized mantle exhumation were found in the northern SCS margin implying that the north of SCS belongs to neither a magma-rich nor magma-poor margin (Ren et al., 2015; Sun et al., 2018; Childress and the Expedition 368X Scientists, 2020). Multichannel seismic data shows that the northern SCS has ultra-wide rifted margins (Pang et al., 2018; Sun et al., 2019; Li et al., 2019), the huge thickness of shallow marine *syn*-rift sediments (Sun et al., 2019), and thick (Cao et al., 2014) and weak (Clift et al., 2002; Sun et al., 2009; Zhang et al., 2020) lower crust. The IODP expeditions proved a rapid transition from the continental breakup to the formation of an igneous oceanic crust (Larsen et al., 2018), suggesting that the mechanism of SCS breakup along the Eurasian plate edge (Cao et al., 2014) differs significantly from that of an ocean, such as the Atlantic. Some studies, therefore, classified SCS into magma-intermediate or even magma-robust margin (Sun et al., 2019; Ding et al., 2020). What drives the rapid transition from rift to drift, and what role does magma play in the thinning process? These questions require further constraints for the crustal structure to reveal the relationship between deep magmatic emplacement and the shallow rifting-breakup deformation and sedimentation.

In this study, we report a new high-resolution OBS profile along the main transect of the central south Pearl River Mouth Basin (PMRB), along which most IODP drill sites are located or surrounded (Fig. 1). Combined with the interpretation of the multichannel seismic data (Profile MCS1555) and analysis of crust thickness, a new model was proposed to illustrate the breakup process of the SCS.

2. Tectonic setting

The South China Sea (SCS) is one of the largest marginal seas in the western Pacific, which has experienced the Mesozoic subduction and the Cenozoic extension. According to the widespread distribution of the subduction-related magmatism on-land and off-land, it has been suggested that that the Paleo-Pacific plate had subducted northwestward beneath the Eurasian plate from the mid-Jurassic to Late Cretaceous (Li and Li, 2007; Li et al., 2018). After the Late Cretaceous, the southeast Eurasian transformed from active subduction to passive extension (Taylor and Hayes, 1983; Cullen, 2014). Numerical modeling suggests that the passive eastern margin was formed by fore-arc splitting, while the western margin was developed by arc separation (Li et al., 2020). Spatial variations in inherited basement structures before the Cenozoic extension may lead to a great variety of rifting structures and breakup patterns across the SCS margin, as well as the significant difference from the margins of the Atlantic. At the northeastern SCS margin (L20 in Fig. 1a), the crust thins from ~25 km beneath the continental shelf to ~12–15 km beneath the distal margin, with ~4 km of crust thickness beneath the continental slope (Lester et al., 2014). The ~3–5 km thick high-velocity lower crust (HVLC) was mainly distributed beneath the distal margin, suggesting either magmatic underplating or pervasive

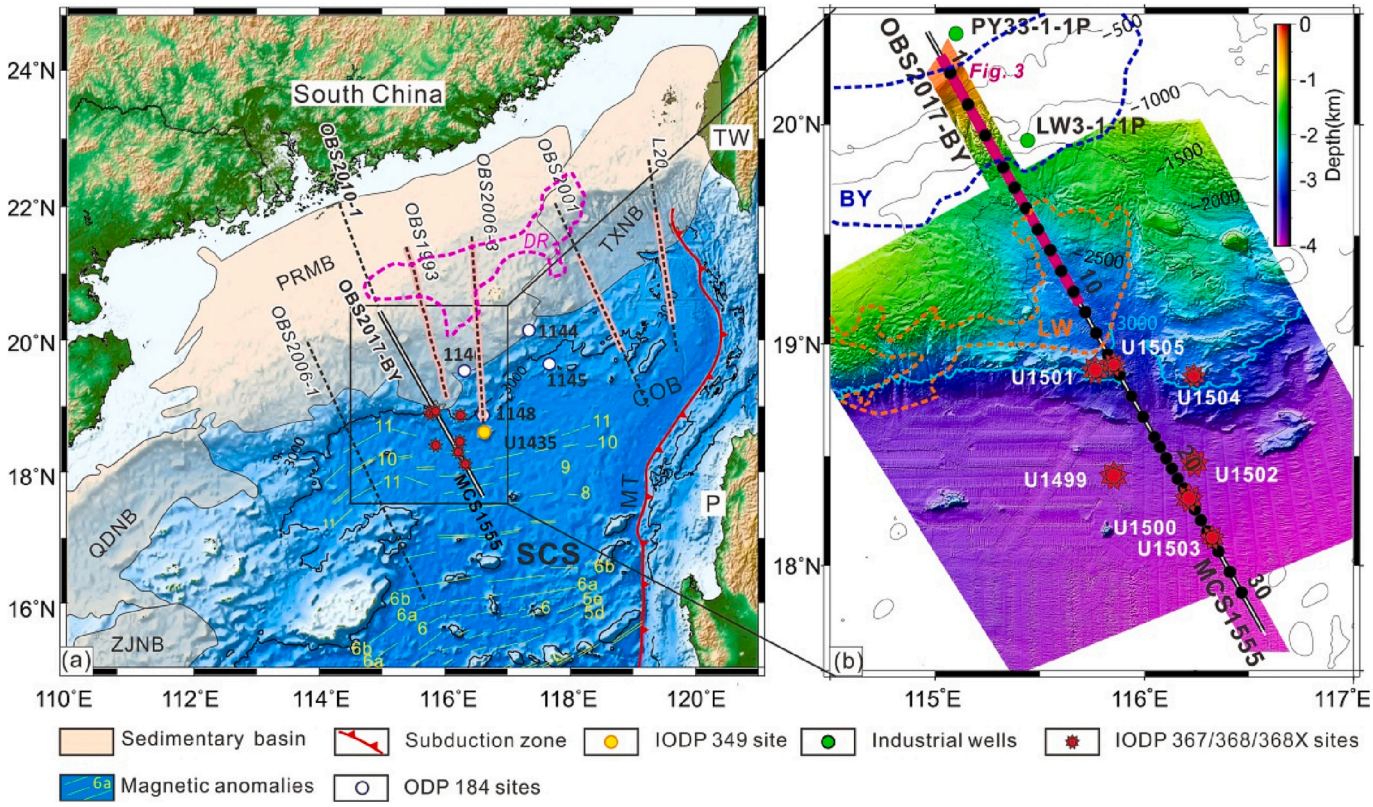

Fig. 1. Regional tectonic map of the study area. (a) Bathymetry map and tectonic features of the northern SCS with the location of OBS2017-BY profile (black bold line), MCS1555 (white thin line along the OBS2017-BY profile) and ODP/IODP sites (Sun et al., 2018; Peate, 1997). Wide-angle seismic profiles are shown as black dashed lines and labeled, OBS1993 (Yan et al., 2001), OBS2001 (Wang et al., 2006), OBS2006–1 (Ding et al., 2012), OBS2006–3 (Wei et al., 2011), OBS2010–1 (Cao et al., 2014) and L20 (Lester et al., 2014). The pink parts of lines are areas with HVLCs. SCS: South China Sea; PRMB: Pearl River Mouth Basin; DR: Dongsha Rise; TXNB: Taixinan Basin; QDNB: Qiongdongnan Basin; ZJNB: Zhongjiannan Basin. MT: Malina Trench; PH: Philippines, TW: Taiwan; Orange dashed boxes correspond to Fig. 7 **(b)** Zoom-in bathymetry map of study area. Black dots represent the OBS locations. The magenta line is the location of the 3D-MCS profile showed in Fig. 3a. The blue and orange dot lines represent the areas of Baiyun Sag (BY) and Liwan Sag (LW), respectively. (For interpretation of the references to colour in this figure legend, the reader is referred to the web version of this article.)

lower crustal intrusions (Lester et al., 2014). At the central northern SCS margin, the crust thickness decreases from ~22 km in the continental shelf (the Dongsha Rise in Fig. 1) to ~8–10 km in the deep sea, with 3–5 km thick HVLC distributed in the base of the lower crust over the shelf and slope (OBS1993 in Fig. 1) (Yan et al., 2001). At northwestern SCS, the crustal thickness is 16–23 km at the continental slope and decreases to ~6 km at the northwest sub-basin (OBS2006–1 in Fig. 1) (Ding et al., 2012). No HVLC was found at the northwestern margin of the SCS (Ding et al., 2012), showing that the crustal structure varies significantly along the northern SCS margin.

The Pearl River Mouth Basin (PMRB) is one of the largest Cenozoic extensional basins located in the central area of the northern SCS margin. Massive thick sediments and faulting structure of the PMRB recorded the rifting process of the SCS margin. The central PRMB developed a margin with a width of ~450 km before breakup occurred at ~30–31 Ma (corresponding to seismic boundary T70) (Zhou et al., 1995; Li et al., 2014; Pang et al., 2007). Its conjugate margin in the south is much narrower, with a width of ~200 km, showing an asymmetric margin (Sun et al., 2009; Franke et al., 2011; Sun et al., 2011). Low-angle detachment faults control >250 km of the central PRMB, and most *syn*-rift faults stop or significantly reduce offset after T83 (~43 Ma) (Zhou et al., 2018; Liu et al., 2019; Zhao et al., 2021). Faults bounding uplifts kept active till around T60 (~24–28 Ma) or even later. Most of the marginal areas were kept in shallow water before T70 but subsided rapidly into deep water after T60 (Jian et al., 2019). Sequence stratigraphy analysis showed that the continental shelf break was located seaward of the Yunli Uplift before the early Miocene and migrated landward to the Baiyun Sag at ~23.8 Ma (Liu et al., 2019). Since the early Miocene, the continental shelf break has been stably situated landward of the Baiyun Sag for a long duration. The Baiyun Sag has been in the same deep-water environment as today (Pang et al., 2018; Zhao et al., 2011).

3. Data and methods

3.1. Data acquisition and seismic phases

The wide-angle seismic refraction profile (OBS2017-BY) (Fig. 1) was collected with 30 ocean bottom seismometers (OBSs), among which 29 were successfully recovered by the *R/V Shiyan 2* in 2017. The OBS array spanned 360 km long with 12–15 km spacing at the Baiyun and Liwan sags and 5–6 km from the COT to the ocean (Fig. 1). The source array consisted of four bolt air guns with a total volume of ~6000 in3 deployed at 10-m water depth. The shooting was conducted at ~250-m intervals to minimize noise contamination from the previous shots. A total of 1567 shots were recorded along the profile. Before seismic phase identification, the OBS data were processed by data transformation (raw data to standard SAC data), time drift and shot point correction, OBS relocation, and band-pass filtering (5–12 Hz), etc. (Liu et al., 2018). Abundant seismic phases were identified and picked according to their kinematic and dynamic characteristics, including *Ps*, *Pg*, *Pn* phases (refractions of the sediment, crust, and upper mantle, respectively), *PsP*, *PcP*, *PmP* phases (reflections of from the sediment bottom, Conrad and crust-mantle boundary, respectively). Following the work of Zelt and Forsyth (1994), the pick uncertainties ranged from 50 to 80 ms (Fig. 2 and Fig. S1 in the supporting information). All OBS phases are shown in Figs. S1–1 to S1–30.

3.2. P-wave velocity modeling

The *P*-wave velocity structures were constrained by both the forward modeling (Zelt and Smith, 1992) and the tomographic inversion (Korenaga et al., 2000) of the seismic traveltimes. The forward modeling was performed using the interactive man-machine method to decrease the misfits between the picked and calculated traveltimes. The model used a combination of multi-beam bathymetry data (Fig. 1b), industrial and IODP drilling results, and the MCS reflection profile (MCS1555)

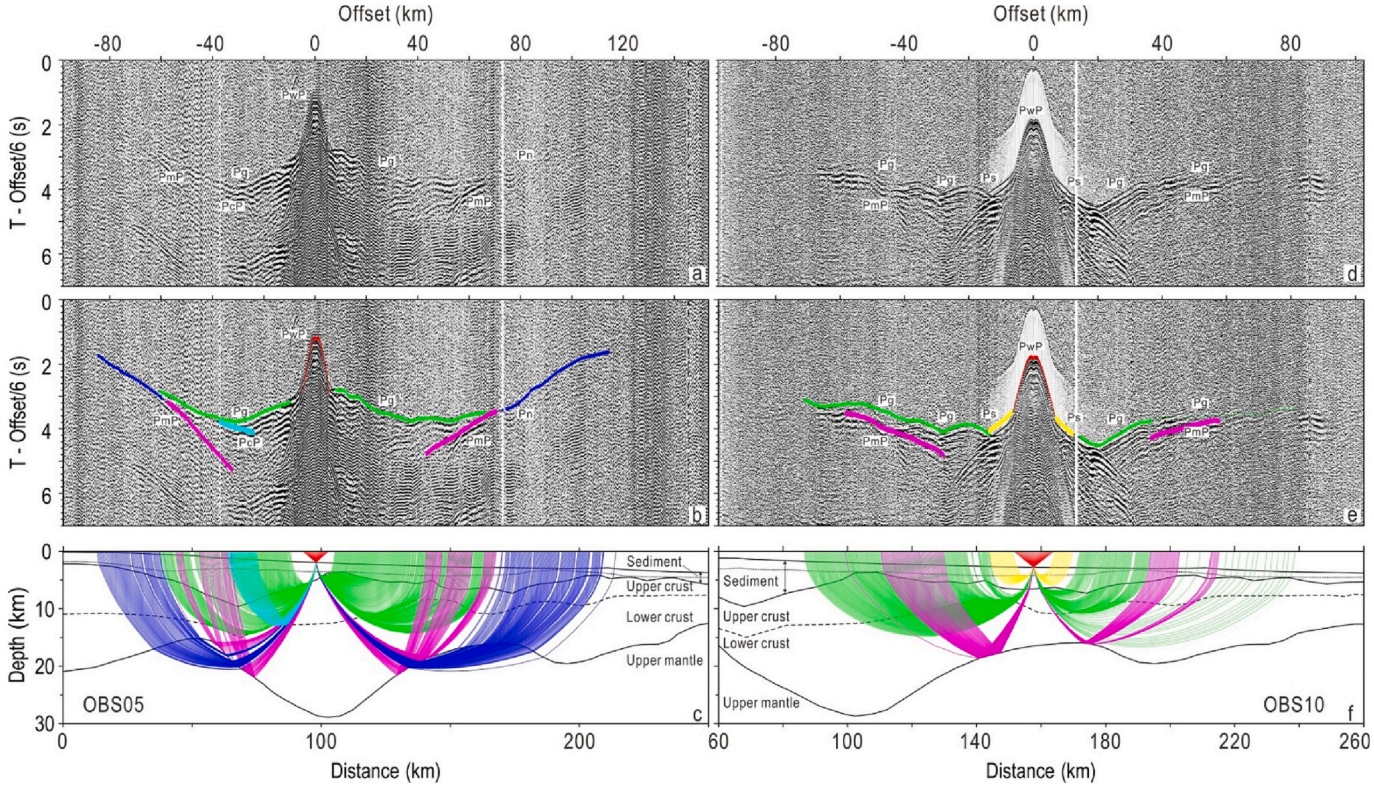

Fig. 2. Interpretations of OBS05 and OBS10. (a) - (c) Original, interpretation of data from OBS05 and seismic ray paths of OBS05. (d) - (e) Original, interpretation of data from OBS05 and seismic ray paths of OBS10.

(Fig. 1) to derive an initial model consisting of a water layer, three sedimentary layers, and crust and mantle layers. Here the MCS data is used to help to constrain the sedimentary structure, including the variation of the basement. Our model contains six layers, including seawater, two sediment layers, the upper crust, the lower crust, and the upper mantle. For the inversion strategy, we constructed an inversion model by the joint refraction and reflection travel-time inversion code *Tomo2D* (Korenaga et al., 2000). In inversion modeling, the geometry of the basement and the sediment velocity were used to help us constrain the initial model, as they are roughly controlled by the *PsP* and *Ps* phases. In the initial model, the crust velocity is set to 5.2 km s^{-1} with a vertical added gradient, and the upper mantle velocity is set to 7.5–8.0 km s^{-1} at a depth of 25 km.

4. Results

4.1. Modeling result and the uncertainty

We manually selected 15,708 first reflections and refraction arrives, and 14,802 phases were used for travel-time fitting (Fig. 3). The final velocity variation ranges of six layers are 1.5 km s^{-1}, 1.8–3.0 km s^{-1}, 3.5–5.4 km s^{-1}, 5.4–6.4 km s^{-1}, 6.4–7.8 km s^{-1}, and 8.0–8.2 km s^{-1}, respectively. The total root means square (RMS) between the picked and calculated traveltimes is 77 ms and the normalized χ^2 is 1.861 for the final model (All RMS and χ^2 were displayed in Table S1 in the supporting information). The initial RMS and normalized χ^2 were 128 ms and 329.40, respectively, while reduced to 76 ms and 1.77 after seven iterations (Fig. 4d).

For the resolution of the final *Tomo2d* model, the checkboard test is used to determine the size of the geological structure that can be

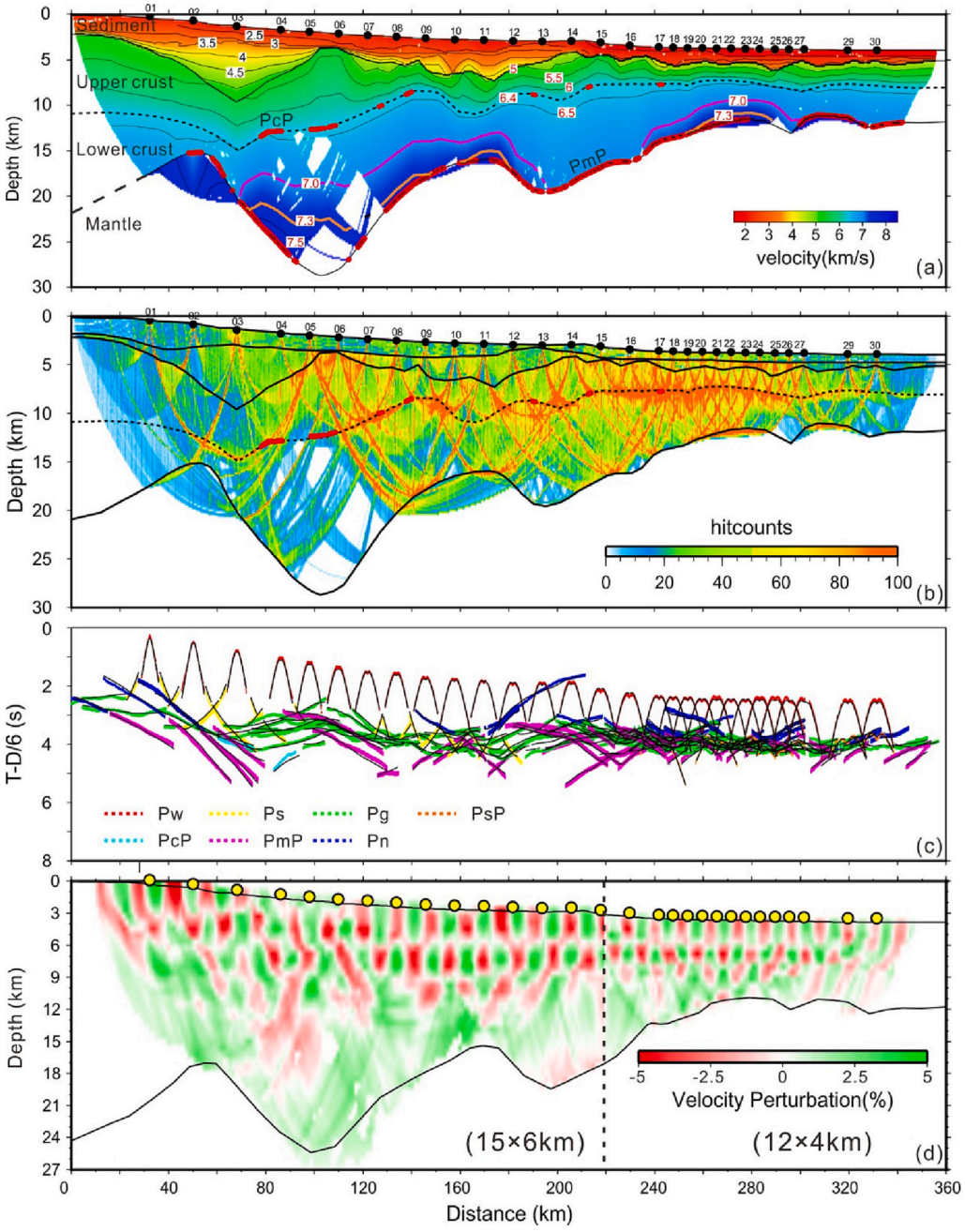

Fig. 3. Forward model and seismic ray paths. (a) Final forward ray-tracing model. The contour is 0.5 km s^{-1} at the region where velocity is below 7.0 km s^{-1} and is 0.2 km s^{-1} at the region where velocity exceeds 7.3 km s^{-1}. (b) Ray coverage density on a 0.4 km × 0.2 km grid corresponding to the above velocity model. (c) All picked (colors) and calculated (black dots) travel-times of the same phases for all of the receivers in the model. (d) Final checkerboard test result with two cell sizes, 15 × 6 km for the landward part and 12 × 4 km for the seaward part.

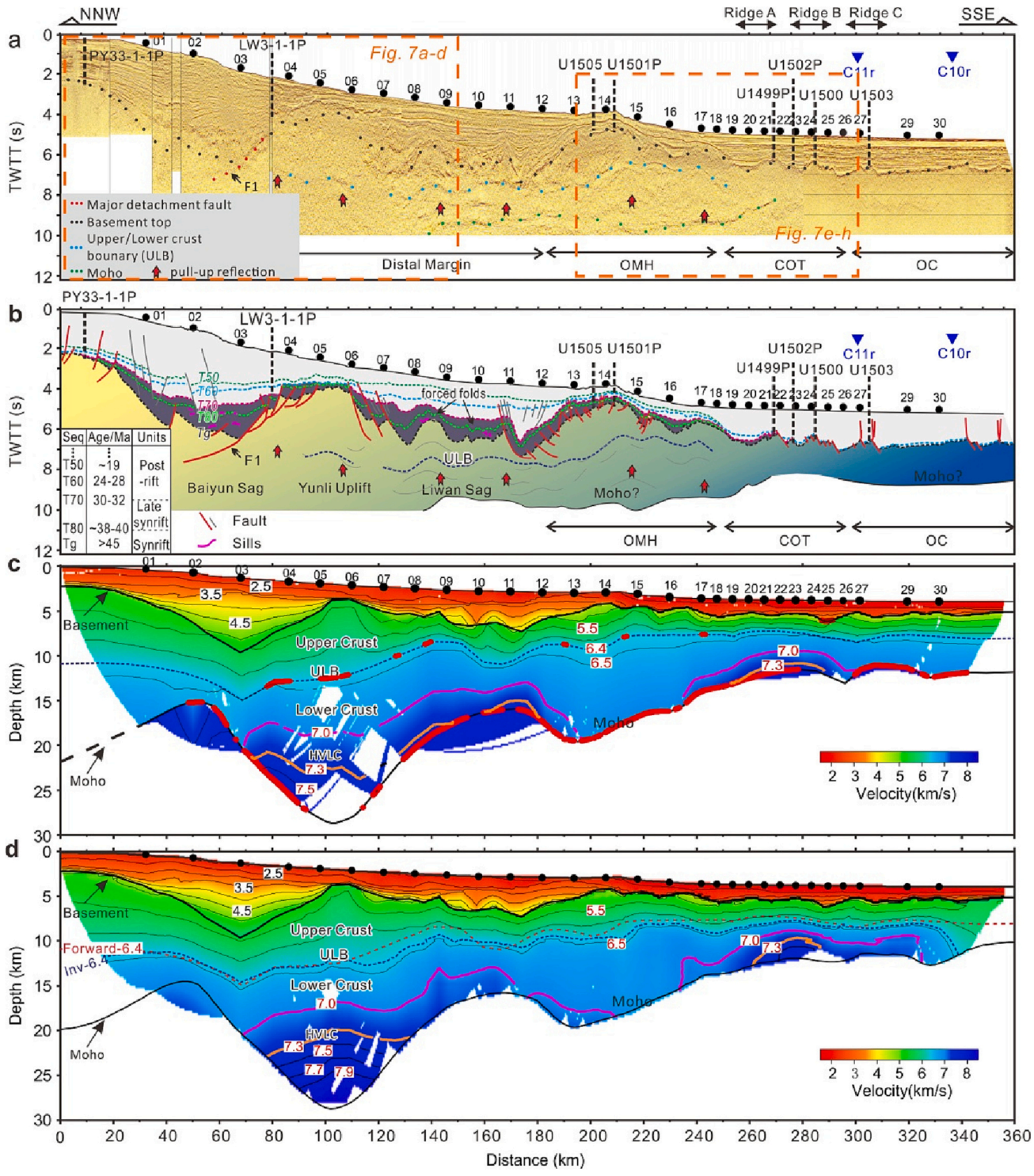

Fig. 4. Interpreted MCS profile, OBS velocity model, and interpreted crustal architecture. (a) Time migration image of the MCS1555 (see location in Fig. 1). OMH: Outer Margin High. COT: Continental Ocean Transition. OC: Oceanic Crust. U1505, U1500, and U1503 are IODP sites drilled directly on the transect, while U1501p, U1499p, and U1502p represent the IODP sites projected to the transect (Sun et al., 2018; Peate, 1997). PY33–1-1p and Lw3–1-1 are industrial drill sites of CNOOC projected to the line (Pang et al., 2018). **(b)** Interpretation of the MCS1555. **(c)** The forward *P*-wave velocity model. The bold red lines represent the areas where Moho and ULB interfaces were constrained by seismic reflection phases, respectively. **(d)** The inverted *P*-wave velocity model. The contour interval is 0.5 km s^{-1} at the region where velocity is <7.0 km s^{-1}, and 0.2 km s^{-1} at the region where velocity > 7.3 km s^{-1}. The Forward-6.4 represents the forward interface between upper and lower crust and the Inv-6.4 represents the inverted interface between upper and lower crust. (For interpretation of the references to colour in this figure legend, the reader is referred to the web version of this article.)

distinguished. In the testing, we first set a velocity perturbation of ±5% for grid nodes to build an input model. The synthetic arrival times calculated with the same source-receiver geometry were then used for the inversion of the output model. The model's resolution can finally be determined by comparing the input and output models.

In our work, different sizes of perturbed cells have been tested, including 20 × 10 km, 15 × 6 km, and 12 × 4 km for horizontal and vertical, respectively (Figs. S2a, b, and c in the supporting information). Because the spaces between OBS stations in the seaward region differ from that in the landward region, we finally chose two cells for our model, 15 × 6 km for the landward part and 12 × 4 km for the seaward part (Fig. 3d and S2c). We conducted a restoring synthetic test to determine the reliability of the high velocity lower crust (HVCL) below the Yunli Uplift (Xia et al., 2018). It shows that the pattern and amplitudes of the input velocity anomalies are recovered well (Figs. S3a and b).

In order to study the detail of the HVCL below the COT, we performed a velocity fluctuation test (Fig. S4). The velocity perturbation is ±1%, and the results show that the velocity of the lower crust below OBS17–27 is higher than in other areas. The velocity of the upper crust below OBS25 and 26 also shows a positive anomaly (high values).

4.2. Crustal structures of the northern margin of the SCS

Both crustal structure and the style of deformation change significantly after passing the major detachment fault F1 and Yunli Uplift. Landward of the Yunli Uplift, rifting is controlled mainly by landward-dipping faults with large vertical offset (Pang et al., 2018; Zhou et al., 2018; Zhao et al., 2018), whereas oceanward of the Yunli Uplift, most *syn*-rift faults dip oceanward and show small vertical offsets (Pang et al., 2018; Zhang et al., 2019). The Moho reflection can be traced below the Liwan Sag to the COT (Figs. 4a and b). The *P*-wave velocity structure (Figs. 4c, d) indicates that the crust thins intermittently from ~20 to ~6 km (Fig. 4) from the shelf to the oceanic basin. The observed *PcP* follows the velocity contour of 6.4 km s^{-1}, usually interpreted as the boundary between the upper and lower crust (ULB). The ULB corresponds well with the semi-continuous wavy reflection discerned on the MCS1555 profile between the basement (Tg) and Moho from the Liwan Sag to the Outer Margin High (OMH) (Fig. 4a).

4.3. HVLC

Two blocks of HVLC with velocity > 7.0 km s^{-1} are observed southward of F1 (Figs. 4c, d). Below the Yunli Uplift, a thick HVLC (~10

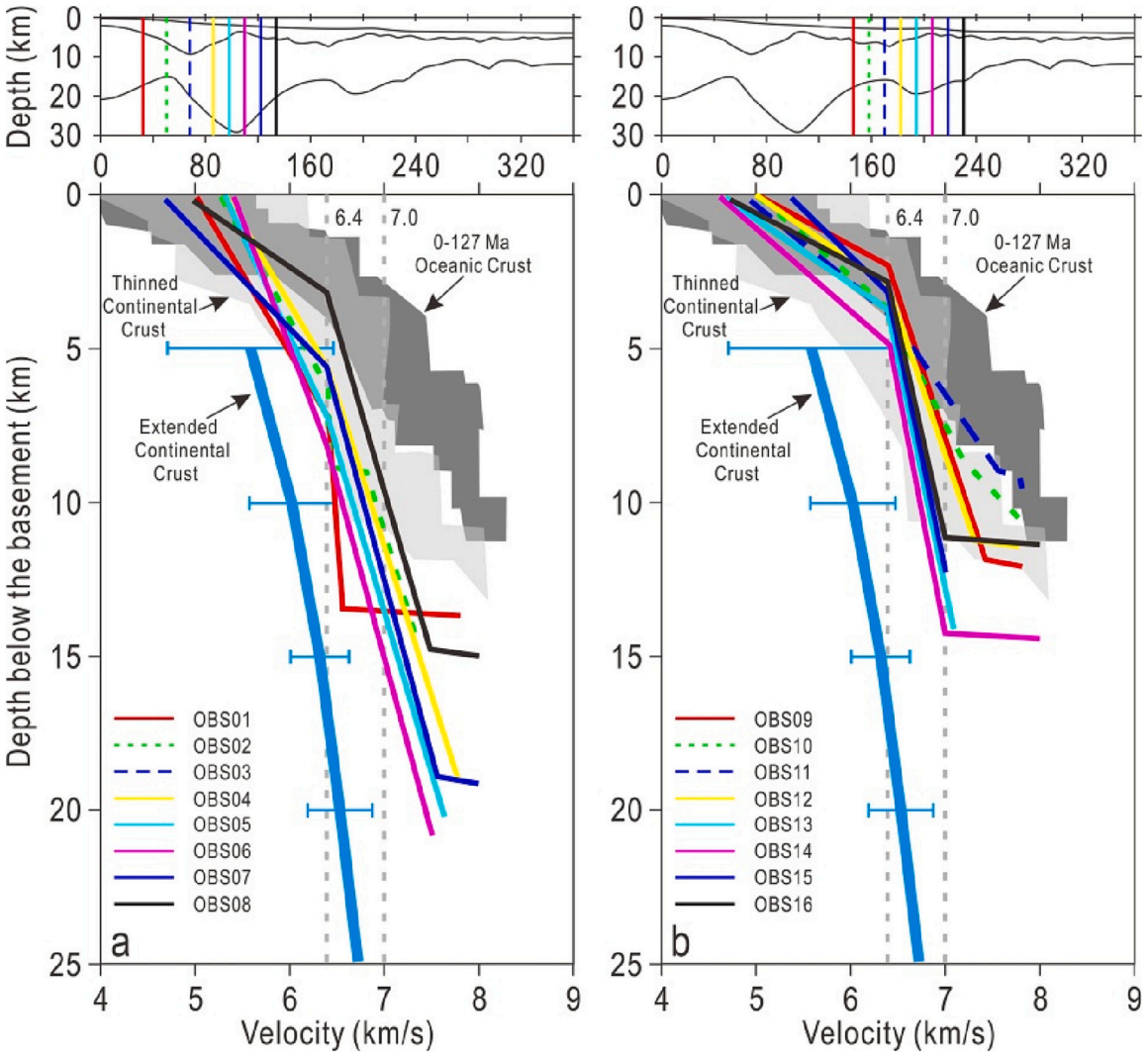

Fig. 5. 1-D velocity-depth profiles (OBS01 - OBS16) extracted from final forward velocity models. Blue lines with uncertainties represent extended continental crust (Christensen and Mooney, 1995). The dark grey area shows the typical velocities for the Atlantic oceanic crust (0–127 Ma) (White et al., 1992), and the light grey area shows the range of velocities for the thinned continental crust at northern margin of the SCS (Nissen et al., 1995; Qiu et al., 2001; Yan et al., 2001; Wang et al., 2006). (For interpretation of the references to colour in this figure legend, the reader is referred to the web version of this article.)

km maximum) is observed below the thickest crust (the present thickness is >25 km) (in the model distance of ~70–210 km in Figs. 4c, d). The bulge shape of the HVLC below the Liwan Sag is consistent with dome structures (in the model distance of ~100–210 km in Figs. 4). The other HVLC with a thickness of ~2–3 km distributes continuously from the southern OMH to the oceanic crust (OC). Three hyper-extended centers are observed below the Baiyun Sag, Liwan Sag, and COT, whereas the thinnest continental crust (~7–8 km) below Baiyun Sag is not accompanied by HVLC (Fig. 4).

5. Discussions

5.1. Variation of the crustal structure

We compared our 1-D velocity-depth results with previous works about the crustal velocity, including velocities of the 0–127 Ma Atlantic oceanic crust (White et al., 1992), the area of SCS thinned continental crust (Nissen et al., 1995; Qiu et al., 2001; Yan et al., 2001; Wang et al., 2006) and the extended continental crust (Christensen and Mooney, 1995) (Figs. 5 and 6; Figs. S5 and S6). The noticeable increase in the velocity gradient from north to south implied a variation from continental to oceanic crust. 1-D velocity profiles from OBS01 to OBS08 were located between the extended and the thinned continental crust (Fig. 5a). From OBS09 to OBS16, the 1-D velocity profiles were almost entirely located in the thinned continental crust area (Fig. 5b). At the seaward side of the OBS16, the margin changes from the thinned continental crust to the oceanic crust gradually (Fig. 6a and b). The inversion velocity results show the similar tendency (Fig. S5 and S6 in the Supporting Information).

It is noteworthy that separated by the OBS 19, velocity on the northern side shows thinned continent crust features with lower 1-D velocity gradient (Fig. 5), while the southern side shows oceanic crust features with high 1-D velocity gradient (Fig. 6). However, matrix-supported breccia and gravels below Tg were recovered by the IODP site U1499P, and the U1502P site recovered altered basalt below Tg. It implies that Ridge A (Fig. 4) records the interaction between late-stage continental extension and breakup-related magmatism (Larsen et al., 2018). Considering the continuation of the continental Moho below Ridge OBS19, we prefer that the1-D velocity profiles from OBS19 to OBS24 reflect the velocity structure of the COT instead of the oceanic crust.

5.2. Geological interpretation of the HVLC

Several wide-angle seismic profiles have been reported along the northern SCS margin (Yan et al., 2001; Wang et al., 2006; Wei et al.,

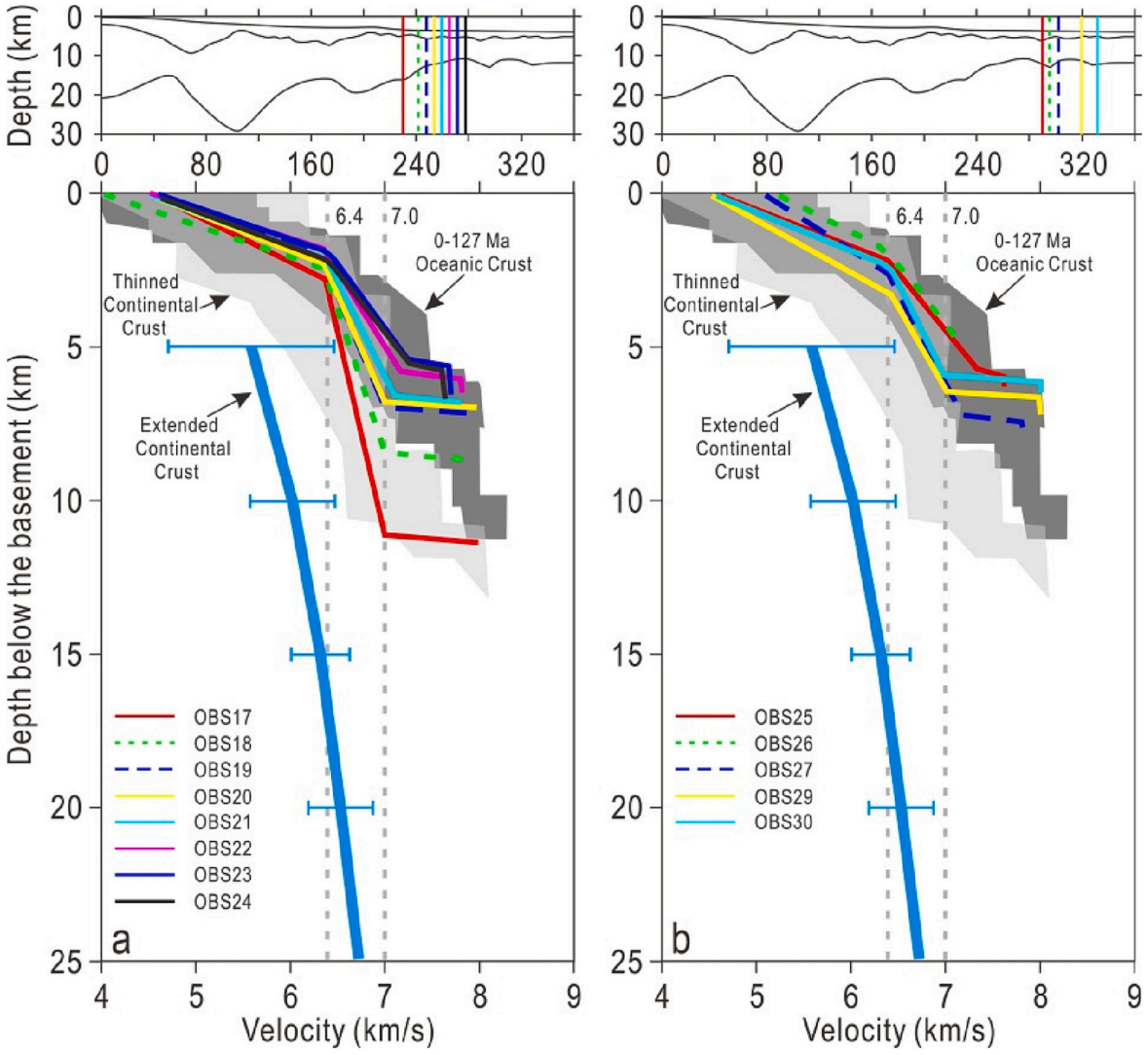

Fig. 6. 1-D velocity-depth profiles (OBS17 - OBS30) extracted from final forward velocity models. The meanings of the colour lines and areas are same as that in Fig. 5.

2011; Ding et al., 2012; Cao et al., 2014; Lester et al., 2014) (Fig. 1), and widespread HVLC is observed in different profiles. Compared with previous results in which the HVLC was regarded as a continuous thick layer (Yan et al., 2001; Wei et al., 2011), the variation of HVLC thickness in this study has higher precision and greater accuracy owing to the smaller station spacing.

The oceanic layer 3 (gabbro) generally has a velocity of 7.0–7.2 km s^{-1}, similar to the HVLC caused by magmatic underplating and intrusion (Yan et al., 2001; Wang et al., 2006; Wei et al., 2011; Ding et al., 2012; Cao et al., 2014; Lester et al., 2014). Therefore, the continent and ocean boundary cannot be discerned from the velocity structure. Both MCS interpretations and gravity inversions (Sun et al., 2019) suggested that ridge C is the starting segment of the steady state OC. In contrast, ridges A and B are transitional crusts that might be composed of thinned continental crust sandwiched by underplated gabbro and erupted basalt (Fig. 4a). The HVLC (velocity > 7.0 km s^{-1}) below the area from the southern OMH to the OC suggests that the lower crust of the COT and some distance landward have become the oceanic crust. HVLC (velocity > 7.3 km s^{-1}) distributes mainly below ridges A and B (Figs. 4b and c), which is consistent with the hypothesis that ridges A and B are

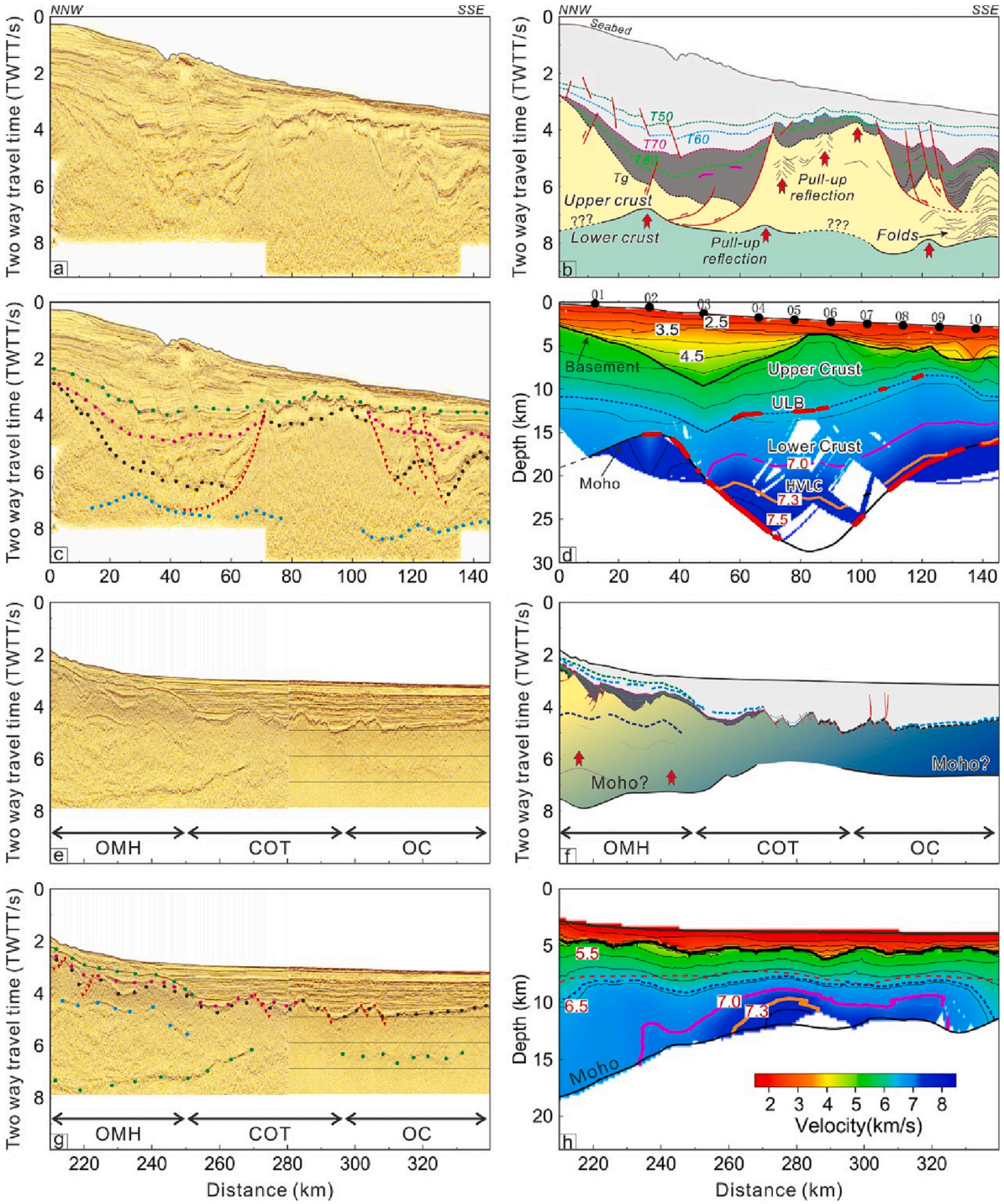

Fig. 7. Details of crustal structure. (a) 3-D MCS profile crossing the Baiyun and Liwan Sags. The location of the profile is showed in Fig. 1b and 4a. (b) - (c) Interpretation of the MCS profile. (d) The corresponding OBS result. (e) 3-D MCS profile crossing the COT. The location of the profile is showed in Fig. 4a. (f) - (g) Interpretation of the MCS profile. (h) The corresponding OBS result.

transitional crusts where underplating magma has time to be geochemically differentiated.

High-amplitude linear features and pull-up reflections are often observed above HVLC in the MCS profile (Figs. 4a, 7), which suggests that the HVLC may be formed by magmatic underplating and intrusion due to that magma has a higher velocity compared with the surrounding crust (Thomson, 2007). For the COT, magmatic underplating should also be the critical mechanism for the HVLC, considering the above-lying diking reflections (Fig. 7e-h) in the crust (Sun et al., 2019) and the basalt encountered at sites U1502, U1500, and U1503 (Jian et al., 2018; Childress and the Expedition 368X Scientists, 2020). Some scientists (Yan et al., 2001; Wang et al., 2006; Wei et al., 2011) suggested that the HVLC might be related to the Plio/Pleistocene magmatism after the cessation of seafloor spreading of the SCS. However Lester et al. (2014) preferred to late stage *syn*-rift or post-rift magmatism. They suggested that the magmatic underplating or intrusion into extended continental crust may be caused by the convective removal of lithospheric mantle and the resulting contact between crust and warm asthenosphere. Sun

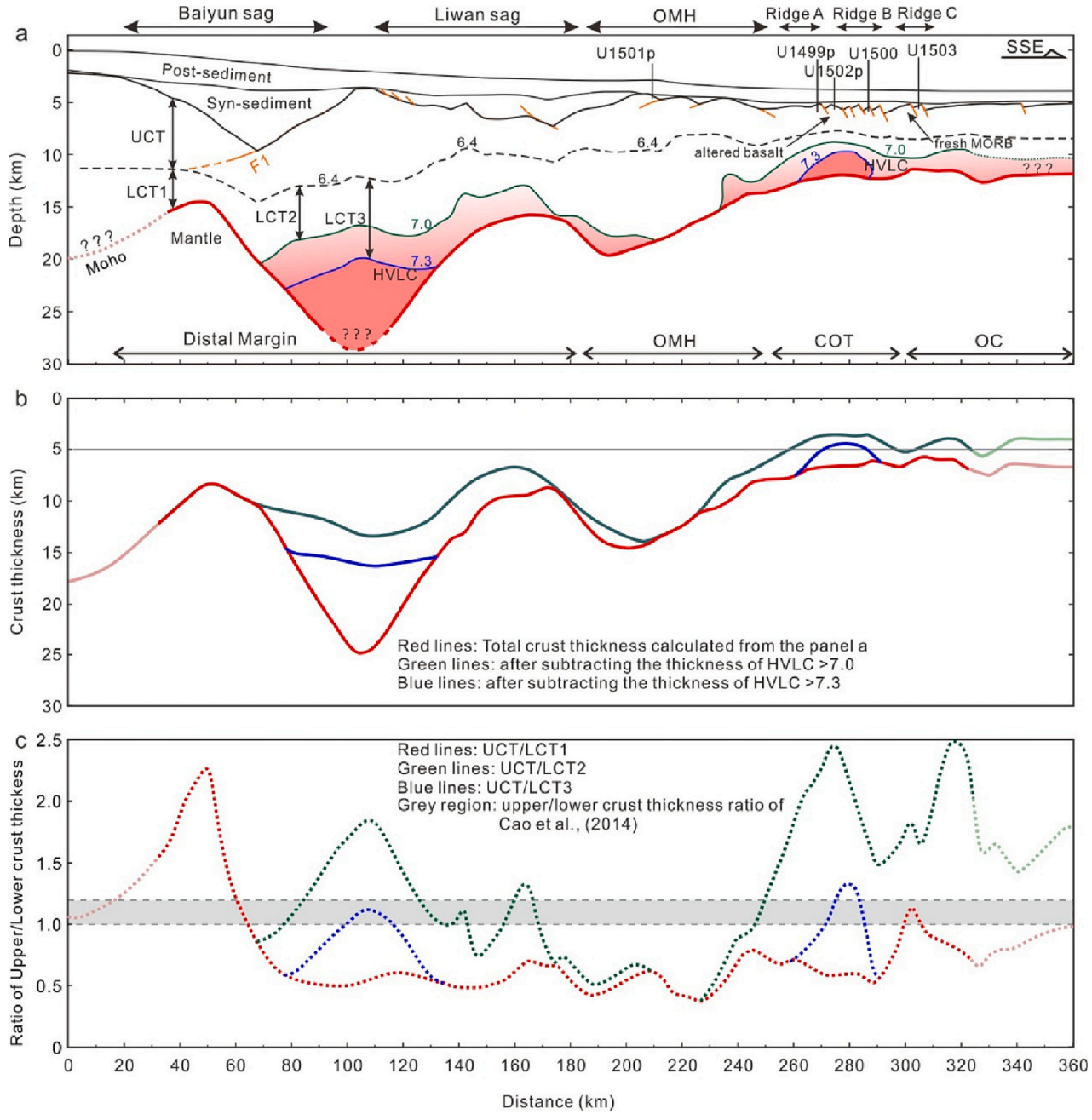

Fig. 8. The crustal structure. (a), thickness (b) and the thickness ratio of upper over lower crust (c) in the northern SCS margin. U1501p, U1499p, U1502p, and U1500 are the IODP sites (Sun et al., 2018). In the panel a, UCT represents the upper crust thickness; LT1 represents the lower crust thickness between the velocity contour of 6.4 km s^{-1} and the Moho; LT2 represents the lower crust thickness between the velocity contours of 6.4 km s^{-1} and 7.0 km s^{-1}; LT3 represents the lower crust thickness between the velocity contours of 6.4 km s^{-1} and 7.3 km s^{-1}. The red solid line in the panel b stands for the present crust thickness, corresponding to the thickness between the basement and the Moho (shown as red-line) in the panel a. The green solid line and the blue solid lines represent the crust thickness after removing the thickness of HVLC, corresponding to the thickness between the basement and the 7.0 km s^{-1} and 7.3 km s^{-1} velocity contours, respectively. The grey region represents the ratio of upper/lower crust thickness along the profile OBS2010–1 (Cao et al., 2014), which has no HVLC. (For interpretation of the references to colour in this figure legend, the reader is referred to the web version of this article.)

et al. (2019) further pointed out that the magmatic process occurred from late rifting to early spreading stages and achieved peak before ~24–28 Ma. The syn-rift magmatism has been also confirmed by well drilling (Pang et al., 2021b). In our study, considering the thick HVLC and the crustal folding deformation, we believe that the HVLC may be related to the syn-rift magmatic underplating.

5.3. Potential causes of thick lower crust

According to previous OBS works in the SCS, the region with a *P*-wave velocity above 6.4 km s^{-1} is considered lower crust. A striking feature of this region is that the lower crust is considerably thicker (Fig. 8a), and the thickness ratio of the upper over lower crust (RULC) is substantially smaller than many other margins (Fig. 8c). Compared with the shelf and inland South China, where the RULC is ~1.2 (Cao et al., 2014), the thick lower crust south of the F1 fault in the distal margin until the COT should be close to this value. However, presuming that the HVLC represents magmatic underplating, the original crustal thickness before magmatic underplating, especially the lower crust thickness is much smaller (Figs. 4 and 8). Especially at the Yunli Uplift, the crustal thickness is reduced to <15–17 km (Fig. 8b). The important mechanism for thick lower crust might thus be magmatic underplating, significantly below the Yunli Uplift and throughout the COT according to the HVLC distribution (Fig. 8b). The other mechanism may be the combined effect of depth-dependent extension and a slight mantle temperature anomaly. Lu and Huismans (2021) suggested that this combined effect can generate melt with thickness over 10 km, which is very close to our observation.

Moreover, Fig. 4 shows that the crustal thinning center is located below the Baiyun Sag, whereas the underplating occurred beneath the area oceanward of the sag center. Suppose underplating correlates with the strongly attenuated mantle lithosphere, as mathematical modeling suggests (Ros et al., 2017). In that case, the mismatch of thinning of the crust and the lithospheric mantle suggests that the ductile lower crust should have served as a decoupling layer between the brittle upper crust and lithospheric mantle.

5.4. Magmatism in the continental margin

In order to study the magmatism in the northern continental margin of the South China Sea (SCS), we compared our observation to melt production in the1-D mantle melting model from the study of Bown and White (1995). Their model estimated melt production under uniformly stretching and lithosphere thinning by assuming stretching factors, rifting durations, and asthenospheric mantle potential temperatures (Bown and White, 1995). Assuming an initial crustal thickness of 35 km (Li et al., 2006), we calculated the stretching factor (McKenzie, 1978) β based on our profile's variation of crustal thickness. Our results showed that β at the Baiyun Sag, Yunli Uplift, and Liwan Sag are 3.9 (green dot in Fig. 9), 3.0 (red dot in Fig. 9) and 4.9 (purple dot in Fig. 9), respectively after excluding the high velocity lower crust (HVLC). The average β of the whole profile is 4.7 (blue dot in Fig. 9).

The rifting started at 45–50 Ma and stopped at ~30 Ma when the SCS began to break up. Therefore, we assume a single rifting episode last 15–20 Myr for simplicity. For these rift durations, the predicted melt thickness changes from 0 to >3 km at different areas for an asthenospheric mantle potential temperature of 1400 °C (Fig. 9). However, when the mantle potential temperature is 1300 °C, none produces any melt (Fig. 9). If the mantle breaks up at ~43–38 Ma in this area and the crust here did not experience noticeable thinning during the late rifting period, the rifting duration is only 2–7 Ma. The predicted melt thickness is <1 km for a potential mantle temperature of 1300 °C. In contrast, it would produce ~2 - ~7 km thickness of melt when the potential mantle temperature of 1400 °C (Fig. 9). We assume that the 2–10 km thick HVLC is an approximate melt thickness. It seems to support a 2–7 Myr rifting duration and a hot (1400 °C according to Bown and White, 1995)

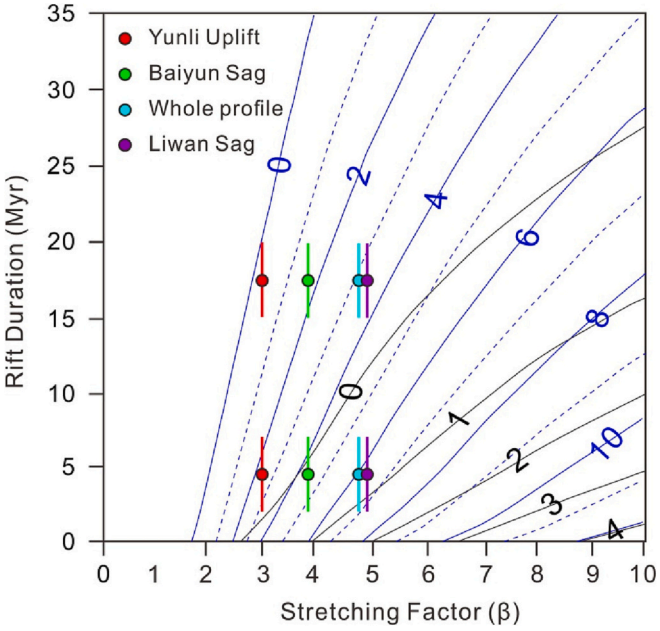

Fig. 9. Predicted melt generation based on the 1-D thermal model of Bown and White (1995). Blue lines is melt production (in km) with a mantle potential temperature 1400 °C, and black lines show melt produced with a 1300 °C asthenospheric mantle. Red, green and purple dots represent the melt productions calculated from crustal stretching factor (β) of the Yunli Uplift, Baiyun Sag and Liwan Sag, respectively. The turquoise dots indicate the melt production calculated from the average crustal stretching factor (β) of the whole profile. (For interpretation of the references to colour in this figure legend, the reader is referred to the web version of this article.)

asthenospheric or a fertile mantle as Ros et al. (2017), Yu et al. (2018) and Sun et al. (2019) implied but not discussed in the text. Therefore, the lithosphere below Yunli Uplift has to be stretched 6–10 times in a short period to generate up to 10 km thick melt. Considering the remnant crustal thickness is still 10–15 km, the mantle below Yunli Uplift has to be strongly attenuated or even broken up in <5 Myr to generate such thick underplating.

5.5. Rifting model of the SCS

The HVLCs are distributed mainly in the east margin of the northern SCS, while less in the west. It is speculated that the eastern margin had been located in the forearc area in the Mesozoic (Li et al., 2018), and therefore the mantle might be more fertile to generate more *syn*-rift magmatism (Sun et al., 2019). However, it is still difficult to explain why huge magma appears below the thick crust (Yunli Uplift) instead of highly extended sags. These observations favor a model with the lithospheric mantle breaking up prior to crust in Baiyun sag at the SCS, considering the decoupling behavior of the crust and the mantle. This model is supported by the industrial drilling at H29, where uplift occurred locally on Yunli Uplift and was accompanied by a volcanic eruption (Pang et al., 2021a). U—Pb dating of the volcanic Zircon indicates ~43 ± 0.5 Ma and 38 ± 0.7 Ma, suggesting that strong magmatic underplating occurred at ~43–38 Ma. According to the crustal structure and corresponding deformation (such as the uplift and rifting of the Yunli Uplift and folds in the Liwan Sag) of the northern SCS margin, we propose that the northern central SCS has experienced two stages of a breakup. The first stage involved mantle breaking up at ~43–38 Ma (T83–T80) (Fig. 10a). Considering the low correlation between the distribution of interpreted magmatism (HVLCs) and the crustal thinning, we infer that the mantle breaking up occurred below the Yunli Uplift. We believe that this stage has little magmatism and the crustal extension is characterized by large detachment faults (such as F1

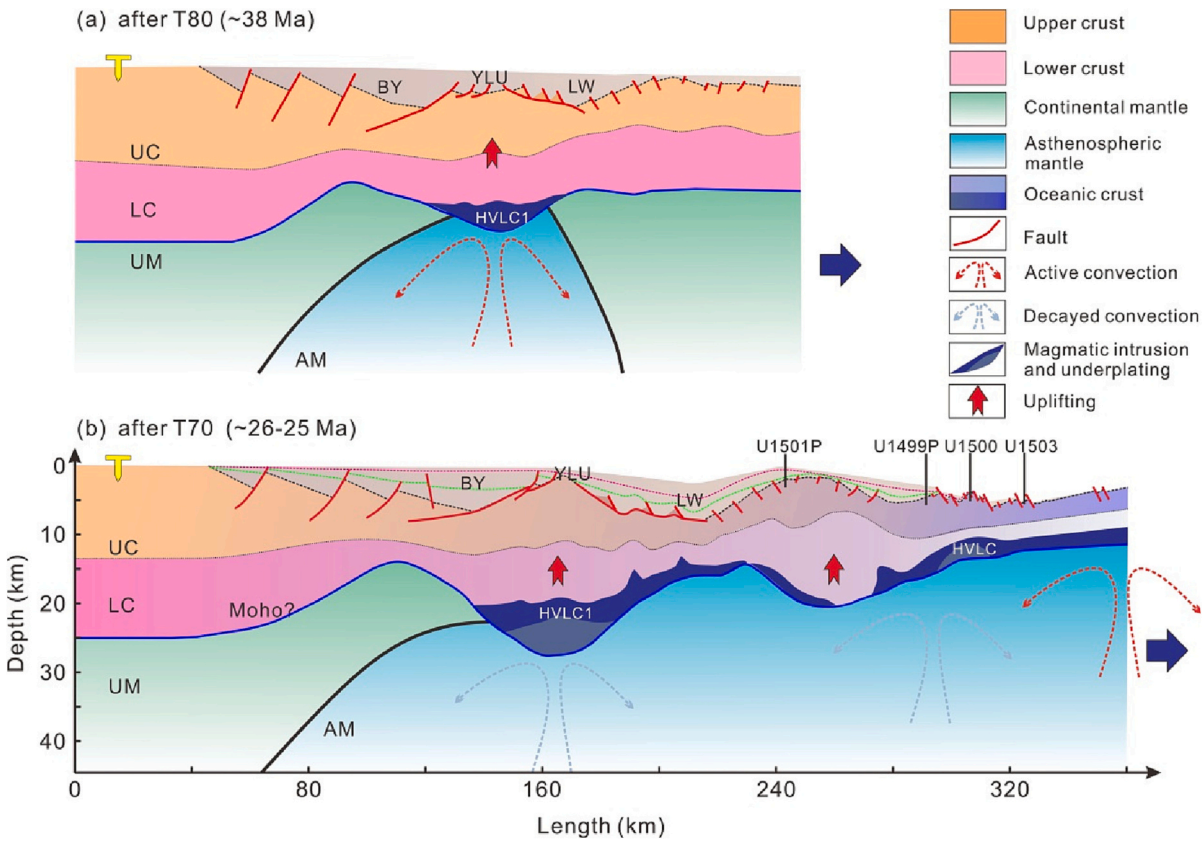

Fig. 10. The rifting and breakup model of the northern continental margin of SCS. (a) After T80 (~38 Ma): the upper lithospheric mantle (UM) was ruptured (or extremely thinned) below the Yunli Uplift in response to strong extension, and caused strong magmatic underplating and intrusion. Before ~38 Ma, detachment and listric normal faults controlled the deformation due to lack of magmatism. **(b)** At ~26–25 Ma, the continental crust has been broken up and the seafloor spreading occurred. The high temperature upwelling may give rise to the crust and generate strong subsidence thereafter. UC: Upper crust. LC: Lower crust. UM: Upper lithospheric mantle. AM: Asthenospheric mantle.

fault in Fig. 4a and b). Meanwhile, passive upwelling of the fertile mantle caused by Mesozoic subduction (Sun et al., 2019) might cause a weak lower crust and resulted in breaking up of lithospheric mantle. The second stage involved crustal breaking up at ~31–29 Ma (T70) (Sun et al., 2019) (Pang et al., 2021b) (Fig. 10b). The crustal breaking up at northeastern margin may occur earlier. Burton-Johnson and Cullen (2022) suggested the breakup back to 41.9 Ma according to the extent of SCS crust subducted at the Manila trench. At this stage, removal of lithospheric mantle placed the margin crust in contact with warm asthenosphere and magmatic processes achieved peak. We speculate that the fertile upwelling may be responsible for the rapid transition from rifting to break up (Larsen et al., 2018).

In summary, owing to the earlier lithospheric mantle breakup, large amounts of magmatic intrusions and underplating could participate in the thinning process oceanward of the lithospheric mantle breakup point, which altered the rifting style, delayed the continental crust breakup by making it ductile and flowable, and decentralized the deformation by generating a new mafic crust below the thinning center.

6. Conclusion

The new seismic velocity model for OBS2017-BY, MCS profile and IODP sites provide constraints on the crustal structure of the central northern margin of the SCS. Our data reveal that the continental margin crust is ~6–20 km thick and detachment faults that sole into the upper crust controlling the distribution of deposit. The thickness of sediments changes from 3 to nearly 10 km, reaching maximum at the Pearl River Mouth Basin.

Two discontinuous HVLCs are found below the distal margin (~10 km) and COT (3–4 km), which may be indicative of magmatic underplating, similar to some of the major structural features observed in the northeastern SCS. Through the analysis of the crust structure, combined with previous age-dating data of drillings, we finally propose a mode with two breakup stages of the SCS in which the first stage is mantle breakup and the second stage is crustal breakup. Lithospheric mantle breakup may occur at ~43–38 Ma below the Yunli Uplift and crustal breakup occurred at ~31–29 Ma below the COT.

CRediT authorship contribution statement

Jiangyang Zhang: Conceptualization, Methodology, Software, Writing – original draft, Data curation, Investigation, Visualization. **Minghui Zhao:** Writing – original draft, Supervision, Data curation, Investigation, Visualization, Project administration. **Zhen Sun:** Conceptualization, Writing – original draft, Supervision, Data curation, Investigation, Visualization, Project administration. **Longtao Sun:** Supervision, Project administration, Data curation, Investigation, Visualization. **Min Xu:** Conceptualization, Supervision, Project administration, Data curation, Investigation, Visualization. **Hongfeng Yang:** Conceptualization, Project administration, Data curation, Investigation, Visualization. **Qiang Wang:** Data curation, Investigation, Methodology, Software. **Xiong Pang:** Writing – original draft, Data curation, Visualization. **Jinyun Zheng:** Writing – original draft, Visualization. **Yongjian Yao:** Writing – original draft, Visualization.

Declaration of Competing Interest

The authors declare that they have no known competing financial

interests or personal relationships that could have appeared to influence the work reported in this paper.

Data availability

Data will be made available on request.

Acknowledgements

The authors are grateful to Andrew Cullen and the other anonymous reviewers for constructive suggestions, and Editor Lin Chen and Weiwei Ding for helpful assistance. The authors thank SCSIO for providing *R/V Shiyan 2* to carry out the OBS2017-BY seismic survey (supported by NSFC Open Research Cruise NORC2017–08), as well as all scientists and sailors involved during the cruise. China National Offshore Oil Corporation-Shenzhen branch and Guangzhou Marine Geological Survey are greatly appreciated for providing MCS profile and multi-beam bathymetry data, respectively. The rock samples and related data were provided by IODP. We are grateful to Dr. Haibo Huang, Siqing Liu, and Fucheng Li for constructive discussion. We thank Enyuan He, Chaoyan Fan, and Ning Qiu for offering technical assistance. GMT (Wessel and Smith, 1995) was used to draw the topographic map.

The research is supported by the National Science Foundation of China (U2244221, 42206071),and Guangdong Special Support talent team Program (2019BT02H594)

Appendix A. Supplementary data

Supplementary data to this article can be found online at https://doi.org/10.1016/j.tecto.2023.229801.

References

Boillot, G., Grimaud, S., Mauffret, A., Mougenot, D., Kornprobst, J., Mergoil-Daniel, J., Torrent, G., 1980. Ocean-continent boundary off the Iberian margin: a serpentinite diapir west of the Galicia Bank. Earth Planet. Sci. Lett. 48, 23–34. https://doi.org/10.1016/0012-821X(80)90166-1.

Bown, J.W., White, R.S., 1995. Effect of finite extension rate on melt generation at rifted continental margins. J. Geophys. Res. 100, 18011–18029. https://doi.org/10.1029/94JB01478.

Burton-Johnson, A., Cullen, A.B., 2022. Continental rifting in the South China Sea through extension and high heat flow: an extended history. Gondwana Res. https://doi.org/10.1016/j.gr.2022.07.015.

Cao, J.H., Sun, J.L., Xu, H.L., Xia, S.H., 2014. Seismological features of the littoral fault zone in the Pearl River Estuary. Chin. J. Geophys. 57, 498–508. https://doi.org/10.6038/cjg20140215.

Childress, L., the Expedition 368X Scientists, 2020. Expedition 368X Preliminary Report: South China Sea Rifted Margin, 2019. International Ocean Discovery Program. https://doi.org/10.14379/iodp.pr.368X.

Christensen, N.I., Mooney, W.D., 1995. Seismic velocity structure and composition of the continental crust: a global view. J. Geophys. Res. 100, 9761–9788.

Clerc, C., Ringenbach, J.C., Jolivet, J., Ballard, J.-F., 2018. Rifted margins: ductile deformation, boudinage, continentward-dipping normal faults and the role of the weak lower crust. Gondwana Res. 53, 20–40. https://doi.org/10.1016/j.gr.2017.04.030.

Clift, P., Lin, J., Barckhausen, U., 2002. Evidence of low flexural rigidity and low viscosity lower continental crust during continental break-up in the South China Sea. Mar. Pet. Geol. 19, 951–970.

Cullen, A., 2014. Nature and significance of the West Baram and Tinjar Lines, NW Borneo. Mar. Pet. Geol. 51, 197–209.

Ding, W.W., Schnabel, M., Franke, D., Ruan, A.G., Wu, Z.L., 2012. Crustal structure across the Northwestern margin of South China Sea: evidence for magma-poor rifting from a wide-angle seismic profile. Acta Geol. Sin. 86, 854–866. https://doi.org/10.1111/j.1755-6724.2012.00711.x.

Ding, W.W., Sun, Z., Mohn, G., Nirrengarten, M., Tugend, J., Manatschal, G., Li, J.B., 2020. Lateral evolution of the rift-to-drift transition in the South China Sea: evidence from multi-channel seismic data and IODP Expeditions 367and368 drilling results. Earth Planet. Sci. Lett. 531, 115932 https://doi.org/10.1016/j.epsl.2019.115932.

Franke, D., Barckhausen, U., Baristeas, N., Engels, M., Ladage, S., Lutz, R., Montano, J., Pellejera, N., Ramos, E.G., Schnabel, M., 2011. The continent-ocean transition at the southeastern margin of the South China Sea. Mar. Pet. Geol. 28, 1187–1204.

Geoffroy, L., Burov, E.B., Werner, P., 2015. Volcanic passive margins: another way to break up continents. Sci. Rep. 5, 14828. https://doi.org/10.1038/srep14828.

Huismans, R., Beaumont, C., 2011. Depth-dependent extension, two-stage breakup and cratonic underplating at rifted margins. Nature. 473, 74–78. https://doi.org/10.1038/nature09988.

Jian, Z., Larsen, H.C., Alvarez Zarikian, C.A., et al., 2018. Site U1505. In: Sun, Z., Jian, J. M. (Eds.), Stock and the Expedition 367/368 Scientists, 367/368. South China Sea Rifted Margin. Proc. IODP. Ch. 9.

Jian, Z.M., Jin, H.Y., Kaminski, M.A., Ferreira, F., Li, B.H., Yu, P.-S., 2019. Discovery of the marine Eocene in the northern South China Sea. Natl. Sci. Rev. 6, 881–885. https://doi.org/10.1093/nsr/nwz084.

Korenaga, J., Holbrook, W.S., Kent, G.M., Kelemen, P.B., Detrick, R.S., Larsen, H.-C., Hopper, J.R., Dahl-Jensen, T., 2000. Crustal structure of the Southeast Greenland margin from joint refraction and reflection seismic tomography. J. Geophys. Res. 105, 21591–21614.

Larsen, H.C., Mohn, G., Nirrengarten, M., et al., 2018. Rapid transition from continental breakup to igneous oceanic crust in the South China Sea. Nat. Geosci. 11, 782–789. https://doi.org/10.1038/s41561-018-0198-1.

Lester, R., Van Avendonk, H.J.A., McIntosh, K., Lavier, L., Liu, C.S., Wang, T.K., Wu, F., 2014. Rifting and magmatism in the northeastern South China Sea from wide-angle tomography and seismic reflection imaging. J. Geophys. Res. Solid Earth 119, 2305–2323. https://doi.org/10.1002/2013JB010639.

Li, Z.X., Li, X.H., 2007. Formation of the 1300-km-wide intracontinental orogen and postorogenic magmatic province in Mesozoic South China: a flat-slab subduction model. Geology. 35, 179–182. https://doi.org/10.1130/G23193A.1.

Li, S., Mooney, W.D., Fan, J., 2006. Crustal structure of mainland China from deep seismic sounding data. Tectonophysics. 420 (1), 239–252. https://doi.org/10.1029/2017JB014861.

Li, C.F., Xu, X., Lin, J., et al., 2014. Ages and magnetic structures of the South China Sea constrained by deep tow magnetic surveys and IODP Expedition 349. Geochem. Geophys. Geosyst. 15, 4958–4983. https://doi.org/10.1002/2014GC005567.

Li, F.C., Sun, Z., Yang, H.F., 2018. Possible Spatial distribution of the Mesozoic Volcanic Arc in the Present-Day South China Sea Continental margin and its Tectonic Implications. J. Geophys. Res. Solid Earth 2018 (123), 6215–6235.

Li, F.C., Sun, Z., Pang, X., Liao, J., Yang, H.F., Xie, H., Zhuo, H.T., Zhao, Z.X., 2019. Low-Viscosity Crustal Layer Controls the Crustal Architecture and thermal distribution at Hyperextended margins: Modeling Insight and Application to the Northern South China Sea margin. Geochem. Geophys. Geosyst. 20, 3248–3267. https://doi.org/10.1029/2019GC008200.

Li, F.C., Sun, Z., Yang, H.F., Lin, J., Stock, J.M., Zhao, Z.X., Xu, H.H., Sun, L.T., 2020. Continental Interior and Edge Breakup at Convergent Margins Induced by Subduction direction Reversal: a Numerical Modeling Study Applied to the South China Sea margin. Tectonics. 39 https://doi.org/10.1029/2020TC006409 e2020TC006409.

Liu, S.Q., Zhao, M.H., Sibuet, J.C., Qiu, X.L., Wu, J., Zhang, J.Z., Chen, C.X., Xu, Y., Sun, L.T., 2018. Geophysical constraints on the lithospheric structure in the northeastern South China Sea and its implications for the South China Sea geodynamics. Tectonophysics. 742-743, 101–119.

Liu, B.J., Pang, X., Wang, J.H., Ren, J., Liu, J., Zheng, J., Xiang, X., Cai, G., Wu, Y., 2019. Sedimentary system response process and hydrocarbon exploration significance of crust thinning zone at extensional continental margin of deep-water area in Pearl River Mouth basin. Acta Petrol. Sin. 40 (S1), 124–138.

Lu, G., Huismans, R.S., 2021. Melt volume at Atlantic volcanic rifted margins controlled by depth-dependent extension and mantle temperature. Nat. Commun. 12, 3894. https://doi.org/10.1038/s41467-021-23981-5.

McKenzie, D., 1978. Some Remarks on the Development of Sedimentary Basins. Earth Planet. Sci. Lett. 40 (1), 25–32.

Nissen, S.S., Hayes, D.E., Buhl, P., et al., 1995. Deep penetration seismic soundings across the northern margin of the South China Sea. J. Geophys. Res. 100, 22407–22433.

Pang, X., Chen, C.M., Peng, D.J., Ming, Z., Yu, S., Min, H., Shen, J., 2007. Sequence stratigraphy of Pearl River Deep-water Fan System in the South China Sea. Earth Sci. Front. 14, 220–229.

Pang, X., Ren, J.Y., Zheng, J.Y., Liu, J., Peng, Y., Liu, B., 2018. Petroleum geology controlled by extensive detachment thinning of continental margin crust: a case study of Baiyun sags in the deep-water area of northern South China Sea. Pet. Explor. Dev. 45, 27–39.

Pang, X., Zheng, J.Y., Mei, L.F., Liu, B.J., Zhang, Z.T., Wu, Z., Feng, X., 2021a. Characteristics and origin of continental marginal fault depressions under the background of preexisting subduction continental margin, northern South China Sea, China. Pet. Explor. Dev. 48, 1237–1250. https://doi.org/10.1016/S1876-3804(21)60106-4.

Pang, X., Zheng, J.Y., Mei, L.F., Liu, B.J., Zhang, Z.T., Wu, Z., 2021b. Structural diversity of fault depressions under the background of preexisting subduction continental margin, Pearl River Mouth Basin, China. Pet. Explor. Dev. 48, 1–11.

Peate, D.W., 1997. The Paraná-Etendeka Province. In: Mahoney, J.J., Coffin, M.E. (Eds.), Large Igneous Provinces in Continental, Oceanic and Planetary Flood Volcanism, Geophys. Monogr. Series, vol. 100, pp. 217–245.

Qiu, X., Ye, S., Wu, S., Shi, X., Zhou, D., Xia, K., Flueh, E.R., 2001. Crustal structure across the Xisha Trough, northwestern South China Sea. Tectonophysics 341, 179–193.

Ren, J.Y., Pang, X., Lei, C., Yuan, L.Z., Liu, J., Yang, L.L., 2015. Ocean and continent transition in passive continental margins and analysis of lithospheric extension and breakup process: Implication for research of the Deepwater basins in the continental margins of South China Sea. Earth Sci. Front. 22, 102–114. https://doi.org/10.13745/j.esf.2015.01.009.

Roberts, D.G., Backman, J., Morton, A.C., Murray, J.W., Keene, J.B., 1984. Evolution of Volcanic Rifted margins: Synthesis of Leg 81 results on the West margin of Rockall Plateau. In: Initial Reports of the Deep Sea Drilling Project 81. Ocean Drilling Program, College Station. https://doi.org/10.2973/dsdp.proc.81.139.1984.

Ros, E., Pérez-Gussinyé, M., Araújo, M., Thoaldo Romeiro, M., Andrés-Martínez, M., Morgan, J.P., 2017. Lower crustal strength controls on melting and serpentinization

at magma-poor margins: potential implications for the South Atlantic. Geochem. Geophys. Geosyst. 18, 4538–4557. https://doi.org/10.1002/2017gc007212.
Sawyer, D.S., Coffin, M.F., Reston, T.J., Stock, J.M., Hopper, J.R., 2007. COBBOOM: the Continental Breakup and Birth of Oceans Mission. Sci. Drill. 5, 13–25. https://doi.org/10.5194/sd-5-13-2007.
Sun, Z., Zhong, Z.H., Keep, M., Zhou, D., Cai, D., Li, X., Wu, S., Jiang, J., 2009. 3D analogue modeling of the South China Sea: a discussion on breakup pattern. J. Asian Earth Sci. 34, 544–556. https://doi.org/10.1016/j.jseaes.2008.09.002.
Sun, Z., Zhao, Z.X., Li, J.B., Zhou, D., Wang, Z.W., 2011. Tectonic analysis of the breakup and collision unconformities in the Nansha. Chin. J. Geophys. 54, 3196–3209.
Sun, Z., Jian, Z.M., Stock, J.M., Larsen, H.C., Briais, A., 2018. South China Sea Rifted Margin. In: Proc. IODP, 367/368.
Sun, Z., Lin, J., Qiu, N., Jian, Z., Wang, P.X., Pang, X., Zheng, J., Zhu, B., 2019. The role of magmatism in the thinning and breakup of the South China Sea continental margin: special Topic: the South China Sea Ocean Drilling. Natl. Sci. Rev. 6, 871–876. https://doi.org/10.1093/nsr/nwz116.
Taylor, B., Hayes, D.E., 1983. Origin and History of the South China Sea Basin. In: Hayes, D.E. (Ed.), The Tectonics and Geologic Evolution Southeast Asian Seas and Islands, Part 2, Geophysical Monograph 27. American Geophysic Union, Washington DC, pp. 23–56.
Thomson, K., 2007. Determining magma flow in sills, dykes and laccoliths and their implications for sill emplacement mechanisms. Bull. Volcanol. 70, 183–201. https://doi.org/10.1007/s00445-007-0131-8.
Wang, T.K., Chen, M.K., Lee, C.S., Xia, K., 2006. Seismic imaging of the transitional crust across the northeastern margin of the South China Sea. Tectonophysics. 412, 237–254. https://doi.org/10.1016/j.tecto.2005.10.039.
Wei, X.D., Zhao, M.H., Ruan, A.G., Lin, Q.X., Yao, H.T., Li, W.Z., Wei, Ao, et al., 2011. Crustal structure of shear waves and its tectonic significance in the mid northern continental margin of the South China Sea, *China*. J. Geophys. 54, 3150–3160. https://doi.org/10.3969/j.issn.0001-5733,2011.12.015.
White, R.S., McKenzie, D., O'Nions, R.K., 1992. Oceanic crustal thickness from seismic measurements and rare earth element inversions. J. Geophys. Res. 97, 19683–19715. https://doi.org/10.1029/92JB01749.
Xia, S.H., Zhao, F., Zhao, D.P., Fan, C.Y., Wu, S.G., Mi, L.J., Sun, J.L., Cao, J.H., Wan, K. Y., 2018. Crustal plumbing system of post-rift magmatism in the northern margin of South China Sea: New insights from integrated seismology. Tectonophysics. 744, 227–238. https://doi.org/10.1016/j.tecto.2018.07.002.
Yan, P., Zhou, D., Liu, Z.S., 2001. A crust structure profile across the northern continental margin of the South China Sea. Tectonophysics. 338, 1–21. https://doi.org/10.1016/S0040-1951(01)00062-2.
Yu, M., Yan, Y., Huang, C.-Y., Zhang, X., Tian, Z., Chen, W.-H., Santosh, M., 2018. Opening of the South China Sea and upwelling of the Hainan plume. Geophys. Res. Lett. 45, 2600–2609. https://doi.org/10.1002/2017GL076872.
Zelt, C., Forsyth, D., 1994. Modeling wide-angle seismic data for crustal structure: Southeastern Grenville Province. J. Geophys. Res. 99, 11,687–11,704. https://doi.org/10.1029/93JB02764.
Zelt, C.A., Smith, R.B., 1992. Seismic travel-time inversion for 2-D crustal velocity structure. Geophys. J. Int. 108, 16–34.
Zhang, C.M., Su, M., Pang, X., Zheng, J., Liu, B., Sun, Z., Manatschal, G., 2019. Tectono-Sedimentary Analysis of the Hyperextended Liwan Sag Basin (Midnorthern margin of the South China Sea). Tectonics. 38, 470–491. https://doi.org/10.1029/2018TC005063.
Zhang, C., Manatschal, G., Pang, X., Sun, Z., Zheng, J., Li, H., Sun, L., Zhang, J., Zhao, Y., 2020. Discovery of mega-sheath folds flooring the Liwan subbasin (South China Sea): Implications for the rheology of hyperextended crust. Geochem. Geophys. Geosyst. 21 e2020GC009023.
Zhao, Z.X., Sun, Z., Xie, H., Yan, C.Z., Li, Y.P., 2011. Baiyun Deepwater Cenozoic subsidence and lithospheric stretching deformation. Chin. J. Geophys. 54, 3336–3343.
Zhao, Y., Ren, J., Pang, X., et al., 2018. Structural style, formation of low angle normal fault and its controls on the evolution of Baiyun Rift, northern margin of the South China Sea. Mar. Pet. Geol. 89, 687–700.
Zhao, Y., Ding, W., Ren, J., et al., 2021. Extension Discrepancy of the Hyper-Thinned Continental Crust in the Baiyun Rift, Northern margin of the South China Sea. Tectonics. 40 (5) e2020TC006547.
Zhou, D., Ru, K., Chen, H.Z., 1995. Kinematics of Cenozoic extension on the South China Sea continental margin and its implications for the tectonic evolution. Tectonophysics. 251, 161–177.
Zhou, Z.C., Mei, L.F., Liu, J., Zheng, J.Y., Chen, L., Hao, S., 2018. Continentward-dipping detachment fault system and asymmetric rift structure of the Baiyun Sag, northern South China Sea. Tectonophysics. 726, 121–136. https://doi.org/10.1016/j.tecto.2018.02.002.